

Revealing the doping density in perovskite solar cells and its impact on device performance

Cite as: Appl. Phys. Rev. **9**, 021409 (2022); doi: [10.1063/5.0085286](https://doi.org/10.1063/5.0085286)

Submitted: 14 January 2022 · Accepted: 30 March 2022 ·

Published Online: 29 April 2022












View Online



Export Citation



CrossMark

Francisco Peña-Camargo,¹  Jarla Thiesbrummel,^{1,2}  Hannes Hempel,³  Artem Musiienko,⁴ 
Vincent M. Le Corre,^{1,5} Jonas Diekmann,¹  Jonathan Warby,¹ Thomas Unold,³  Felix Lang,¹ 
Dieter Neher,¹  and Martin Stolterfoht^{1,a)} 

AFFILIATIONS

¹Physik weicher Materie, Institut für Physik und Astronomie, Universität Potsdam, Karl-Liebknecht-Str. 24-25, 14776 Potsdam, Germany

²Clarendon Laboratory, University of Oxford, Parks Road, Oxford OX1 3PU, United Kingdom

³Department of Structure and Dynamics of Energy Materials, Helmholtz-Zentrum Berlin für Materialien und Energie, D-14109 Berlin, Germany

⁴Institut für Silizium-Photovoltaik, Helmholtz-Zentrum Berlin für Materialien und Energie, Kekuléstrasse 5, 12489 Berlin, Germany

⁵Institute of Materials for Electronics and Energy Technology, Friedrich-Alexander-Universität Erlangen-Nürnberg, 91058 Erlangen, Germany

Note: This paper is part of the special collection on Energy Storage and Conversion.

^{a)}Author to whom correspondence should be addressed: stolterf@uni-potsdam.de

ABSTRACT

Traditional inorganic semiconductors can be electronically doped with high precision. Conversely, there is still conjecture regarding the assessment of the electronic doping density in metal-halide perovskites, not to mention of a control thereof. This paper presents a multifaceted approach to determine the electronic doping density for a range of different lead-halide perovskite systems. Optical and electrical characterization techniques, comprising intensity-dependent and transient photoluminescence, AC Hall effect, transfer-length-methods, and charge extraction measurements were instrumental in quantifying an upper limit for the doping density. The obtained values are subsequently compared to the electrode charge per cell volume under short-circuit conditions (CU_{bi}/eV), which amounts to roughly 10^{16} cm^{-3} . This figure of merit represents the critical limit below which doping-induced charges do not influence the device performance. The experimental results consistently demonstrate that the doping density is below this critical threshold ($\sim 10^{12} \text{ cm}^{-3}$, which means $\ll CU_{bi}/eV$) for all common lead-based metal-halide perovskites. Nevertheless, although the density of doping-induced charges is too low to redistribute the built-in voltage in the perovskite active layer, mobile ions are present in sufficient quantities to create space-charge-regions in the active layer, reminiscent of doped pn -junctions. These results are well supported by drift-diffusion simulations, which confirm that the device performance is not affected by such low doping densities.

Published under an exclusive license by AIP Publishing. <https://doi.org/10.1063/5.0085286>

INTRODUCTION

Traditionally, many inorganic semiconductor devices, such as transistors, photodetectors, light-emitting diodes, and solar cells, are based on electrical junctions created by electronic doping. Doping of semiconductors is generally achieved by the introduction of atoms with higher (lower) valency than the substituted atoms, which creates free electrons (holes) in the conduction (valence) band, thereby increasing (lowering) the Fermi level of the semiconductor. The dark concentration of carriers determines the position of the Fermi level. For substitutional doping in inorganic semiconductors, dopants are,

for example, introduced by vapor-phase epitaxy. This allows us to tune their concentration with high precision, reaching concentrations up to 10^{20} cm^{-3} for GaAs (Ref. 1), Ge, crystalline Si (Ref. 1), and amorphous Si (Refs. 2 and 3). In solution-processed semiconductors such as organic semiconductors, on the other hand, dopants can be introduced by adding molecules with very-low-lying lowest unoccupied molecular orbital (LUMO) energy levels for p -doping or, conversely, very-high-lying highest occupied molecular orbital (HOMO) energy levels for n -doping.^{4–8} In general, doping can also originate from the creation of free extra carriers upon the formation and ionization of defects.⁹

Such defects can be intrinsic (vacancies, interstitials, or substitutions) or extrinsic (impurities), and from their activation energy, they can be shallow (close to band) or deep (close to the middle of the bandgap). Shallow defects can donate electrons to the conduction band or accept electrons from the valence band, creating free holes in the latter. Conversely, deep defects do not donate carriers to bands but act as recombination centers or traps, thus limiting the performance of any semiconductor device. This highlights that charge defects and doping are closely related, and thus the same rules apply for the detection of both, which is linked to the surface charge density on the electrodes. In this respect, Kirchartz and co-workers recently showed that the detection of a charged defect concentration from electrical measurements is not possible with electrical measurements if the concentration is significantly below the electrode charge density.^{10,11} This has far reaching implications for the reported defect densities in perovskite systems, which might be much smaller than expected (potentially comparable to the densities obtained in single crystals^{10,11}).

In contrast to crystalline inorganic semiconductors, doping of the absorber layer is a more controversial topic in perovskites. For example, the community refers to perovskite solar cells as having a *pin* or *nip* architecture, which underlines that the active layer is expected to be intrinsic.¹² On the other hand, several publications suggested that perovskites are strongly doped, with reported densities as high as 10^{20} cm^{-3} (Refs. 13–17). Moreover, in a previous study, the improved solar cell performance was attributed to the formation of an apparent *pn*-homojunction in the absorber layer (reminiscent of Si solar cells), even though the obtained doping densities were rather low ($<10^{13} \text{ cm}^{-3}$) (Refs. 11 and 18). The controversy with regard to whether lead-halide perovskites behave as intrinsic semiconductors or not, is a result of various aspects:

- (a) Doping is often referred to as a mere addition of certain additives to the precursor solutions. Although additives may dope a material in a chemical sense, this does not mean that the material is also electronically doped. The use of the word *doping* without clarifying its type contributes to the controversy. From here on, we will refer to the *doping density* as the concentration of free majority charge carriers in the perovskite layer in the dark.
- (b) Electronic doping can be achieved by the introduction of intrinsic defects in the perovskite ABX_3 lattice.¹² The presence of both donor and acceptor shallow defects was previously demonstrated in MAPbI_3 single crystals.¹⁹ Density Functional Theory (DFT) calculations show the possibility of tailoring doping densities as a consequence of defect formation.²⁰ Changing the ratio PbX_2/AX in the fabrication procedure can induce intrinsic defects, and some studies reported doping densities in the order of 10^{18} cm^{-3} achieved in this way.¹⁷ However, further experimental evidences point to a general limitation for carrier densities of MAPbI_3 at $<10^{14} \text{ cm}^{-3}$ for both stoichiometric and non-stoichiometric compositions.^{18,21,22}
- (c) Photoemission spectroscopy measurements often suggest an apparent *p*- or *n*-type perovskite layer. However, charge transfer and charge redistribution give rise to an energetic alignment of the Fermi level of the perovskite and the substrate, causing a shift of the energy levels and associated band bending.²³ Consequently, depending on the substrate, different conclusions

might be obtained with respect to the doping of the perovskite layer, as was recently shown by Shin *et al.*²⁴ Furthermore, although several groups have observed an *n*-type perovskite surface, this does not imply that the bulk is doped, as ultraviolet photoemission spectroscopy measures only the energetics at the surface.^{25–27} To quantify the band bending within the perovskite absorber layer or the bottom interface, surface photovoltage (SPV) measurements can be performed using white background light. Upon saturation of the valence band onset with light intensity, the bands are flattened, thereby revealing the energy levels of the bulk. Indeed, for a triple cation perovskite $\text{Cs}_{0.05}(\text{FA}_{0.83}\text{MA}_{0.17})_{0.95}\text{Pb}(\text{I}_{0.83}\text{Br}_{0.17})_3$ on a typical hole transport layer, these measurements have demonstrated that the Fermi level in the perovskite bulk is close to midgap^{25–27} (see the [supplementary material](#), Fig. S1 for further details). Even though perovskites were found to be highly doped in several publications on photoemission spectroscopy (e.g., Ref. 28), the numerical value of the doping density is often not specified. In addition to the classification of perovskites as doped semiconductors depending on the position of the Fermi level, future studies should estimate the doping density to evaluate if it is significant enough to influence the device performance, or if the semiconductor can be considered as effectively intrinsic for solar cell operation.

- (d) High concentrations of mobile ions between 10^{15} and 10^{19} cm^{-3} have been reported for lead halide perovskites,^{29–33} and the ion-induced field-redistribution could be misinterpreted as redistribution of doping-induced electrons or holes.
- (e) Mott–Schottky (MS) plots are widely used to evaluate the doping density. However, the interpretation of the data is not straightforward. In particular, the MS analysis should be applied to doped semiconductors in the bias region where the depletion width is smaller than the device thickness d (Refs. 34–36). For perovskite systems with an active layer thickness of 400 nm and a built-in potential U_{bi} of 1 V (Ref. 37), this implies that at least 10^{16} cm^{-3} free charges must be present in the device to evaluate the doping density using the MS analysis. Another equivalent definition at which the doping density matters can be introduced by considering the charge on the electrodes, which will be discussed in this paper.

Generally, the doping density can be directly assessed or with techniques that require complementary characterization, as recently summarized by Euvrard *et al.*¹² Techniques, such as four-point-probe,³⁸ transfer-length method,³⁹ and van der Pauw,⁴⁰ are used to evaluate the doping density via the electrical conductivity, assuming a constant mobility.⁴¹ The evaluation of the doping density is also possible using Hall effect measurements and Mott–Schottky analysis. However, as mentioned previously, the interpretation of the latter is not straightforward, especially in low-doped and very thin films, where the doping of the active layer cannot be disentangled from injected charges from the contacts and recombination.^{34,42} For semiconductors with low mobility ($\leq 1 \text{ cm}^2 \text{ V}^{-1} \text{ s}^{-1}$) and high resistivity ($\geq 10^6 \Omega \text{ cm}$), the Hall effect has to be measured in an alternative way to the static configuration due to the poor signal-to-noise ratio. Lock-in detection and AC magnetic fields are used to overcome this issue.^{19,21,43} In addition, doping can be also investigated indirectly, for example, via intensity dependent photoluminescence quantum efficiency⁴⁴ (PLQY) or

via pump-probe spectroscopy by means of, e.g. transient photoluminescence (TRPL)⁴⁵ and time-resolved microwave conductivity.⁴⁶ Charge extraction techniques, such as Bias-Assisted Charge Extraction (BACE),⁴⁷ space-charged-limited currents,⁴⁸ and Charge Extraction by Linearly Increasing Voltage (CELIV)⁴⁹ are also known to be suitable for quantifying the doping density of organic,³⁵ inorganic,⁴⁹ and perovskite solar cells.⁵⁰ We also note that some methods, such as PLQY, charge extraction, and Mott-Schottky, are more limited than Hall effect measurements in terms of sensitivity, i.e., it may only be possible to obtain an upper limit of the doping density if the doping concentration is very low.

In this study, we investigate and quantify the electronic doping density for a range of six different sorts of lead-halide perovskites by several highly sensitive and reliable methods. To obtain the free carrier density in the dark, Hall effect measurements were performed in a van der Pauw square arrangement with four-contacts with an alternating current (AC) magnetic field (50 mHz) and a lock-in amplification to enhance the Hall signal. The determined free carrier densities are on the order of 5×10^{11} – $3 \times 10^{13} \text{ cm}^{-3}$. Furthermore, we used transistor-like structures to evaluate the conductivity of thin films through the transfer length method (TLM) in the dark. In the corresponding neat films, we measured the intensity-dependent PLQY to compare the trend of the experimental data with a recombination model. This approach yields an upper limit for the doping-induced charge density on the order of 10^{12} cm^{-3} . These results are further confirmed by TRPL measurements, which also demonstrate a density below $2 \times 10^{12} \text{ cm}^{-3}$ for a triple cation Pb-based perovskite. We then performed CELIV measurements in the dark to investigate the doping in complete devices. In addition, intensity-dependent photo-CELIV was measured to demonstrate the sensitivity of the CELIV method and to support the conclusions drawn from these measurements. Finally, we corroborated these results with drift-diffusion simulations to highlight that the device performance is not affected by the measured densities of doping-induced charge.

RESULTS

To generalize the findings, our investigated set of perovskites is composed of archetypal methylammonium lead iodide MAPbI₃, a double cation/mixed halide Cs_{0.15}FA_{0.85}Pb(I_{0.75}Br_{0.25})₃, and four different triple cation Cs_{0.05}(FA_{*x*}MA_{*y*})_{0.95}Pb(I_{*x*}Br_{*y*})₃ perovskites with various concentrations of formamidinium lead iodide FAPbI₃ (*x*) and methylammonium lead bromide MAPbBr₃ (*y*). For all these compositions, thin neat films, transistor-like structures, and full devices were fabricated. In addition, neat perovskite samples, in the van der Pauw configuration with gold contacts, were prepared for Hall effect measurements. The structure of the full devices follows a *pin*-architecture comprising ITO (150 nm)/PTAA:PFN-Br (8 nm)/perovskite (400 nm)/C₆₀ (30 nm)/BCP (8 nm)/Cu (100 nm)], where ITO is indium-doped tin oxide, PTAA is poly[bis(4-phenyl)(2,4,6-trimethylphenyl)amine], PFN-Br is poly[(9,9-bis(30-((N,N-dimethyl)-N-ethylammonium)-propyl)-2,7-fluorene)-alt-2,7-(9,9-dioctylfluorene)] dibromide, and BCP is bathocuproine (further details are provided in the [supplementary material](#) Methods). Their corresponding *JV* curves are shown in the [supplementary material](#) Fig. S2. A summary of the photovoltaic parameters is also shown in the [supplementary material](#) Fig. S3. Before introducing the experimental methods to quantify the doping density, we discuss at which concentrations, electronic doping becomes relevant for solar cell performance.

When does the doping density matter?

Kirchartz and Cahen have recently discussed that for a *pn*-junction to be formed, the doping density should be above approximately 10^{16} cm^{-3} (Ref. 51). In addition to this explanation, a simple threshold at which the doping density becomes relevant for the device performance can be obtained as follows.

Let $C = \epsilon_0 \epsilon_r S/d$ be the geometrical capacitance of a solar cell, where S is its area, ϵ_0 is the permittivity of free space, and ϵ_r is the relative dielectric constant of the absorber layer. When such a cell is short-circuited, a charge equivalent to $C U_{bi}$ will be accumulated on its electrodes. This quantity, divided by the cell volume V and the elementary charge e , with an active layer thickness of 400 nm, is on the order of 10^{16} cm^{-3} for perovskite systems.^{51,52} As long as their density is significantly below $C U_{bi}/eV$, the impact of doping-induced equilibrium charges on the internal built-in field will be negligible. Consequently, the device operation would not be affected. The results of drift-diffusion simulations, displayed in [Fig. 1](#), are consistent with these basic considerations. These simulations, which have been tailored to describe efficient triple cation perovskite solar cells, as discussed in our previous work,³⁷ demonstrate that the doping-induced charges will only redistribute the internal field at densities higher than 10^{16} cm^{-3} . Moreover, this rule of thumb holds regardless of the type of doping, whether it is *n* or *p*. The corresponding *JVs* for a range of donor (n_0) doping densities are shown in [Fig. 1\(a\)](#), whereas those for a range of acceptor densities (p_0) are shown in [Fig. 1\(b\)](#). In both cases, the device performance is adversely impacted when $n_0, p_0 \geq 10^{16} \text{ cm}^{-3}$. However, doping can be beneficial in a specific density regime as recently discussed.⁵³ For example, in [Fig. 1\(a\)](#), we observe a slightly beneficial effect in the case of a *n*-doped active layer with a density of around 10^{15} cm^{-3} . In this case, the reason is an improved hole extraction to the hole-transport layer, which lowers the hole density in the active layer and the carrier density at the critical *n*-interface. More general aspects under which conditions doping in the active layer can be beneficial were discussed in Refs. 51 and 53.

To show that increasing the doping density beyond $C U_{bi}/eV$ causes a redistribution of the internal field, [Fig. 1\(c\)](#) represents the band diagram at a device bias of 0 V for some acceptor doping densities simulated with the same parameters used in [Fig. 1\(b\)](#). As a conclusive criterion, the electrode charge density $C U_{bi}/eV$ marks the critical density at which doping matters. We note that this concept is generally valid for thin-film solar cells, although the capacitance is inversely dependent on the film thickness. Therefore, $C U_{bi}/eV$ depends inversely on the square of the active layer thickness of the solar cell (d^{-2}). Notwithstanding these points, it is an interesting question, whether the presence of mobile ions in perovskites, with densities reported in the literature ranging from 10^{15} to 10^{20} cm^{-3} (Refs. 30–33), can influence this criterion. To check this statement, we performed additional simulations, with a mobile cation density of 10^{17} cm^{-3} , the same number of immobile anions, and variable doping densities. *JV* curves and the corresponding band diagrams at zero bias for both acceptor and donor densities are shown in the [supplementary material](#) Fig. S7. In the case of mixed polarities of ionic and dopant species [[supplementary material](#) Fig. S7(b)], a deviation from the $C U_{bi}/eV$ criterion is observed, i.e., doping only starts to matter if the doping density is comparable to the ion density ($10^{17} \text{ cm}^{-3} > C U_{bi}/eV$). To investigate the influence of ion densities in the absence of doping, we have simulated *JV* curves and band diagrams at zero

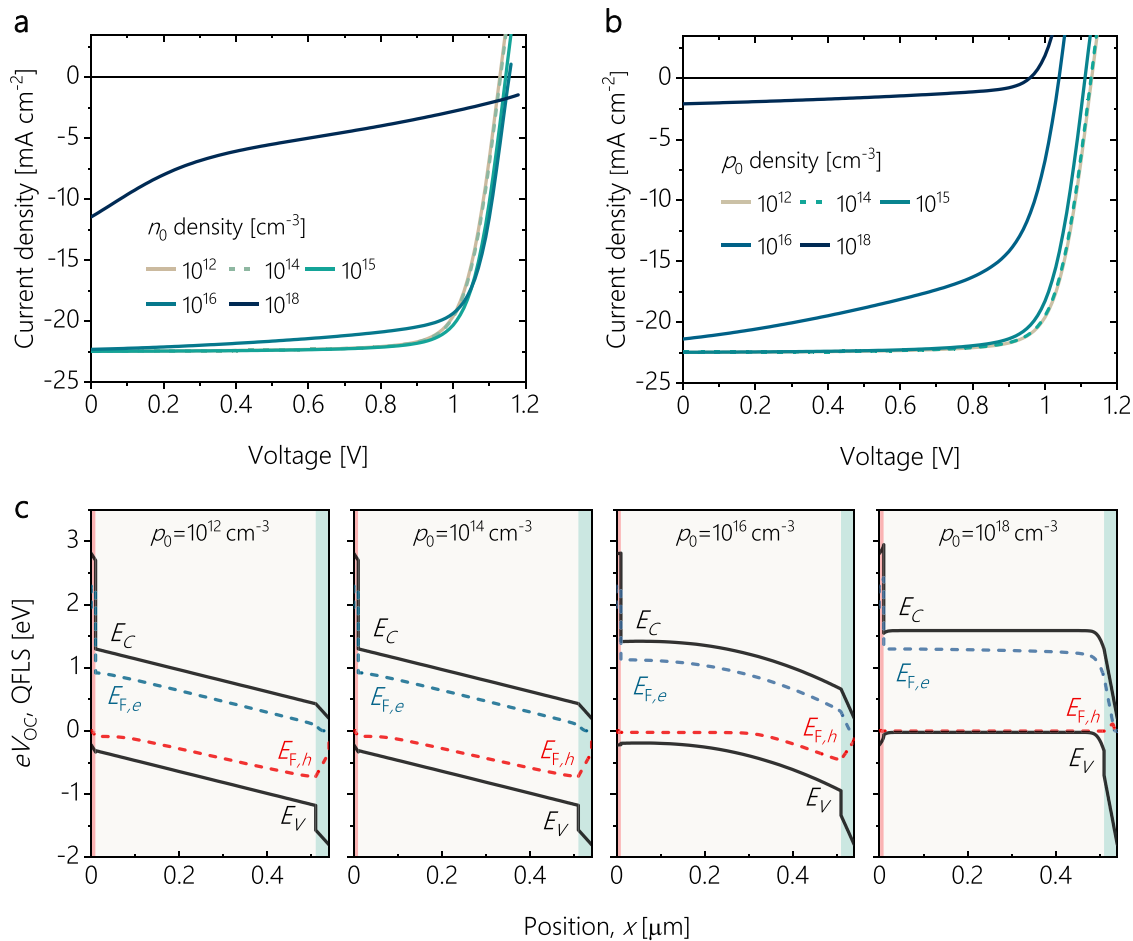


FIG. 1. Current density vs voltage curves simulated using SCAPS (a Solar Cell Capacitance Simulator)^{54,55} without mobile ions as a function of the doping by (a) donors (n_0) and (b) acceptors (p_0). Below the CU_{bi}/eV charge density (approximately 10^{16} cm⁻³), the doping density has no influence on the device performance. (c) Corresponding band diagrams at zero voltage for various acceptor doping densities without mobile ions. Simulations with mobile ions can be found in the [supplementary material](#) Fig. S7.

bias when the doping density is set to zero and the ion density varies. The result of this simulation is shown in [supplementary material](#) Fig. S8. The mobile cation density is varied from 10^{14} to 10^{18} cm⁻³ while the same number of anions are kept immobile. In this case, the CU_{bi}/eV criterion holds for variable ion densities, i.e., when the ion density is higher than 10^{16} cm⁻³, the device performance starts being affected.

Hall effect, transfer length method, and conductivity

Hall effect measurements enable us to determine the carrier concentration by means of probing the interaction of the charge carriers with an applied magnetic field. Samples were prepared in the traditional van der Pauw layout⁴⁰ with four gold contacts placed at the corners of a square-shaped perovskite film.

Figure 2(a) shows the measured Hall carrier density for the studied compositions. Although the values are different for the different perovskites, the free electron densities in the dark n_0 are in the range of 5×10^{11} – 3×10^{13} cm⁻³. We assign this carrier density to the doping-

induced charge. The corresponding value for MAPI (1.9×10^{12} cm⁻³) is in good agreement with results of Hall effect measurements reported in literature.²¹ As Hall effect is driven by a magnetic field that deviates the trajectory of the carriers depending on their velocities and charge type, heavy charges (like ions) would not be that fast to react to the magnetic field. The contribution of mobile ions to the Hall signal is estimated to be less than 0.2%. The ionic contribution is hence negligible compared to that of highly mobile free carriers.^{32,56–58} This is further discussed in [supplementary material](#) Note S2.

The sample conductivity in the dark σ was assessed by three different measurements. On the same films used for Hall effect, a voltage was applied to two opposite-located contacts and the current is measured. The results are displayed in Fig. 2(b) with the label “2c.” The second approach relies on the use of the four contacts at a time, i.e., the voltage is applied to two neighboring contacts and current is collected in the remaining two. The outcome is also shown in Fig. 2(b) under the label “4c.”

Finally, it is also possible to estimate the electrical conductivity of a neat perovskite film using the so-called transfer length method based

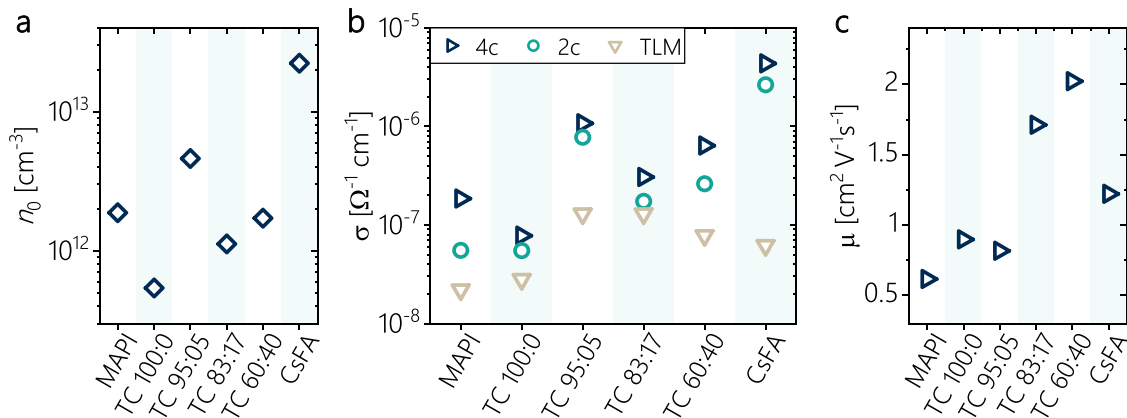


FIG. 2. (a) Free charge carrier density in the dark n_0 determined by AC Hall effect measurements for the six different perovskites. Here, “CsFA” refers to $\text{Cs}_{0.15}\text{FA}_{0.85}\text{Pb}(\text{I}_{0.75}\text{Br}_{0.25})_3$ and “TC” stands for Triple Cation perovskites $\text{Cs}_{0.05}(\text{FA}_x\text{MA}_y)_{0.95}\text{Pb}(\text{I}_x\text{Br}_y)_3$ with different percentages of formamidinium lead iodide FAPbI_3 (x) and methylammonium lead bromide MAPbBr_3 (y), displayed in the graphs as TC x:y. (b) Conductivity values extracted from the three described methods: four contacts in the van der Pauw configuration (4c), average of the two two-opposite contacts (2c) and transfer length method (TLM). (c) Calculated mobilities using the expression $\mu = \sigma_{4c}/(en_0)$, where σ_{4c} is the conductivity obtained using the four contacts in the van der Pauw layout as shown in (b).

on a transistor-like device structure.³⁹ The working principle, measurement scheme and device architecture are discussed in the [supplementary material](#) Note S1. All the perovskite compositions were analyzed in the same way and the obtained conductivities are shown in [Fig. 2\(b\)](#) under the label of “TLM.” [Figure 2\(b\)](#) shows that the transfer length method gives lower values of the conductivity for all the compositions in comparison with the other two approaches.

Hereafter, the mobility μ is calculated from the conductivity and the carrier density using the equation $\mu = \sigma/(en_0)$, where e is the elementary electronic charge. The results are shown in [Fig. 2\(c\)](#) for the different compositions and they lie between 0.5 and $2.5 \text{ cm}^2 \text{V}^{-1} \text{s}^{-1}$, which is in good agreement with values reported in the literature obtained with the same approach.^{18,21,43} In this case, the conductivities used for the calculations are those determined by the four-contact approach, i.e., $\sigma = \sigma_{4c}$. As σ_{4c} is the highest value among the three conductivity sets, the mobilities calculated using the other conductivity sets would be lower. The numerical values of the quantities represented in [Fig. 2](#) are listed in the [supplementary material](#) Table S1, including the calculated intrinsic carrier concentration n_i for every composition. As the conductivity and the carrier density were measured independently and are linearly related, it is expected that the compositions with a high carrier density, have a higher electrical conductivity. This can be seen in [Figs. 2\(a\)](#) and [2\(b\)](#) and it holds approximately for the conductivities obtained from “4c” and “2c.” Therefore, normalizing these conductivities and the carrier densities to those of one of the compositions (e.g. TC 100:0), yields a consistent trend which is shown in the [supplementary material](#) Fig. S4. In both van der Pauw configuration and TLM layout, charge transport occurs in-plane. Therefore, not only does the transport depend on the size of the crystallites and on the abundance and nature of the grain boundaries, but also it is different from the transport in vertical direction within a single crystal as expected in thin films.⁵⁹

Nevertheless, from the results of Hall effect measurements, we can estimate that the density of doping induced charge is in the range of 1×10^{11} to $4 \times 10^{13} \text{ cm}^{-3}$. This means that doping density

is still far below the critical threshold of the electrode charge density ($CU_{bi}/eV \approx 10^{16} \text{ cm}^{-3}$) as discussed above. Likewise, assuming a $U_{bi} = 1 \text{ V}$ and calculating the depletion width as discussed by Kirchartz and Cahen,⁵¹ a depletion width of about $10 \mu\text{m}$ is obtained, exceeding the actual active layer thickness of $0.4 \mu\text{m}$.

Intensity-dependent photoluminescence quantum yield

As the recombination of the charge-carriers is influenced by doping, it is possible to indirectly quantify the doping density by means of TRPL and intensity-dependent PLQY measurements.^{45,60,61} The total recombination rate R_{tot} can be written as $R_{\text{tot}} = -d(\Delta n)/dt = k_2 \Delta n(\Delta p + p_0) + k_1 \Delta n$, where $\Delta n = \Delta p$ are the photogenerated (excess) electron and hole carrier densities, respectively, and k_2 and k_1 are the radiative and non-radiative coefficients, respectively. The Auger coefficient has been excluded as it plays a minor role under 1 sun equivalent illumination conditions, and an acceptor doping density p_0 has been introduced.^{60,62} The external PLQY is given by $Q_e^{\text{lum}} = J_{\text{rad}}/J_{\text{tot}} = J_{\text{rad}}/(J_{\text{rad}} + J_{\text{non-rad}})$, where, in terms of their corresponding recombination rates, the radiative and non-radiative recombination current densities are $J_{\text{rad}} = e d R_{\text{rad}}$ and $J_{\text{non-rad}} = e d R_{\text{non-rad}}$, respectively. Hence,

$$Q_e^{\text{lum}} = \frac{k_2 \Delta n(\Delta n + p_0)}{k_2 \Delta n(\Delta n + p_0) + k_1 \Delta n}. \quad (1)$$

Equation (1) can be plotted as a function of Δn , which, in turn, is related to the intensity (in suns equivalent) by the following expression:

$$k_2 \Delta n(\Delta n + p_0) + k_1 \Delta n = \frac{J_{\text{gen}}}{ed} = \frac{\phi J_{\text{SC}}}{ed}, \quad (2)$$

where J_{gen} is the generation current density, ϕ is the intensity in suns, n is the total electron carrier density (in this case, $n = \Delta n$), and J_{SC} is the implied short-circuit current density at 1 sun. From the Q_e^{lum}

values as a function of the intensity, the total carrier density n can be calculated as follows:

$$n^2 = n_i^2 \exp\left(\frac{\Delta E_F}{k_B T}\right), \quad (3)$$

where k_B is the Boltzmann constant, T is the absolute temperature and the quasi-Fermi level splitting, and ΔE_F is determined as

$$\Delta E_F = k_B T \ln\left(Q_e^{\text{lum}} \frac{J_{\text{gen}}}{J_{0,\text{rad}}}\right). \quad (4)$$

Here, $J_{0,\text{rad}}$ is the maximum recombination current density in the dark and J_{gen} depends on the intensity via Eq. (2). The analytical expression (1) is plotted in Fig. 3(a) as a function of the illumination intensity and the corresponding total carrier density, from Eq. (3), is shown in Fig. 3(c).

As the light intensity, and thereby the generated carrier concentration, decreases ($\Delta n \ll p_0$), Q_e^{lum} levels off at different values depending on the doping density p_0 . In this regime, first-order recombination dominates and consequently Q_e^{lum} does not longer depend on the charge carrier density. From a physical point of view, this leveling out of Q_e^{lum} at low intensities is because one of the Fermi levels is pinned by the

doping concentration and therefore only one of the Fermi levels shifts with the photogenerated carrier concentration. Above $\Delta n = p_0$, both Fermi levels shift with the increasing carrier concentration, which leads to a steeper increase in ΔE_F and, therefore, of Q_e^{lum} . Figure 3(a) further shows that as the doping density increases, and Q_e^{lum} levels out at higher intensities. The same trend against the carrier density is shown in the supplementary material of Ref. 44. The recombination coefficients used in the Figs. 3(a) and 3(c), were previously quantified for a triple cation perovskite $\text{Cs}_{0.05}(\text{FA}_{0.83}\text{MA}_{0.17})_{0.95}\text{Pb}(\text{I}_{0.83}\text{Br}_{0.17})_3$ and they are $k_1 = 2 \times 10^6 \text{ s}^{-1}$ and $k_2 = 3 \times 10^{-11} \text{ cm}^3 \text{ s}^{-1}$ (Ref. 37). Similar trends can be demonstrated for MAPi, where recombination coefficients $k_1 = 5 \times 10^6$ and $k_2 = 8.1 \times 10^{-11} \text{ cm}^3 \text{ s}^{-1}$ (Ref. 64) were used.

Experimentally, Q_e^{lum} can be measured for different light intensities. A neat perovskite film, initially kept in the dark, is illuminated with a 520 nm-wavelength-laser whose intensity can be systematically varied by means of a filter wheel. Figure 3(b) shows the experimental results for the different perovskite films where the light intensity was varied from low to high. Additionally, the trend of the total carrier density against the intensity is shown in Fig. 3(d) calculated using Eq. (3) and the data in Fig. 3(b). The expected carrier density n is of the order of 10^{15} cm^{-3} at 1 sun, which matches very well with the results reported in the literature.²⁵

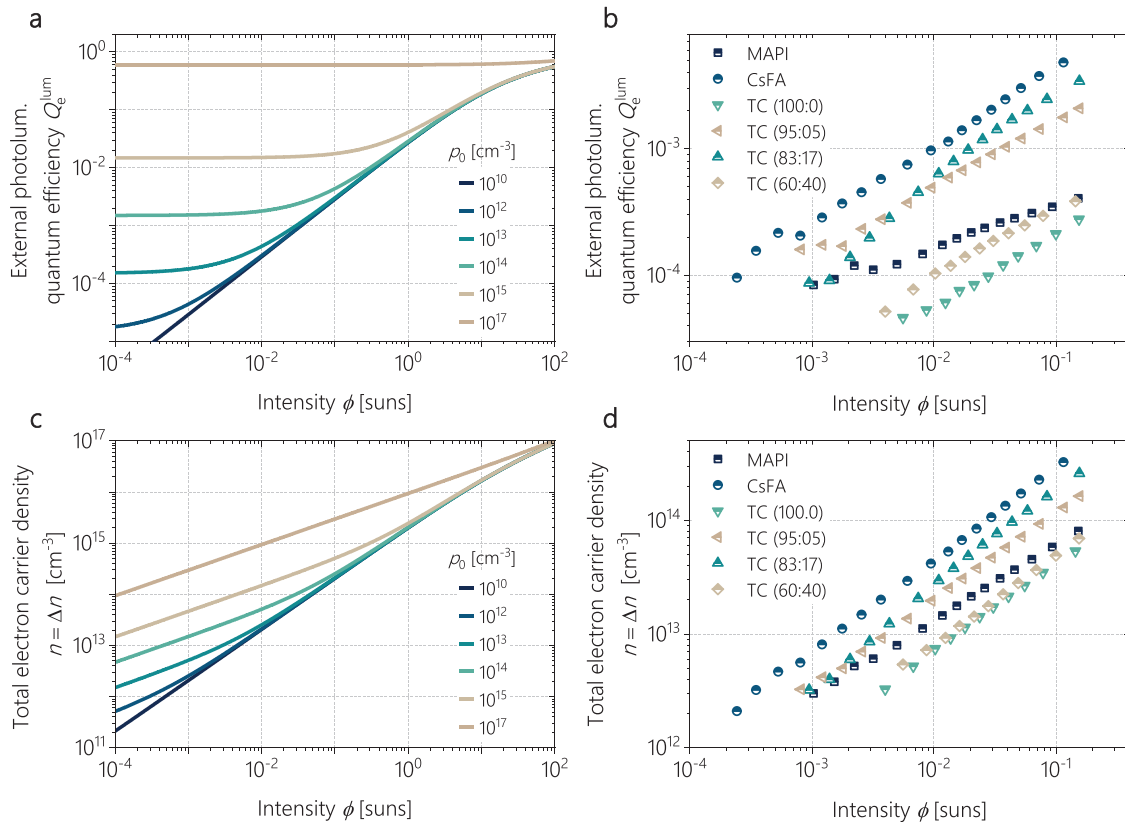


FIG. 3. (a) Q_e^{lum} as a function of the light intensity ϕ in suns equivalent for different doping densities p_0 according to the model of the Eq. (1) with the constants $k_1 = 2 \times 10^6 \text{ s}^{-1}$ and $k_2 = 3 \times 10^{-11} \text{ cm}^3 \text{ s}^{-1}$ (Ref. 37) for a triple cation perovskite $\text{Cs}_{0.05}(\text{FA}_{0.83}\text{MA}_{0.17})_{0.95}\text{Pb}(\text{I}_{0.83}\text{Br}_{0.17})_3$. (b) Experimental data for the studied compositions, where the light intensity was changed from low to high. (c), total carrier density for $\text{Cs}_{0.05}(\text{FA}_{0.83}\text{MA}_{0.17})_{0.95}\text{Pb}(\text{I}_{0.83}\text{Br}_{0.17})_3$ for different doping densities calculated using Eq. (3) and the same constants used for (a). (d) Experimental total carrier density n computed using expression (3) and the data from (b).

As Q_e^{lum} depends on the emissive properties of the material, Q_e^{lum} values below 10^{-5} are already in the detection limit of our setup, therefore, the number of experimental points is different for the range of perovskite compositions. According to Fig. 3(d), this sensitivity limit corresponds to an excess carrier density of $2 \times 10^{12} \text{ cm}^{-3}$. Hence, from these measurements on these samples, $2 \times 10^{12} \text{ cm}^{-3}$ constitutes an upper limit for the doping density in all cases. This outcome is consistent with the electrical conductivity and Hall effect measurements.

Time-resolved photoluminescence amplitude

For continuous illumination, the carrier concentration can be estimated by Eq. (3) or (4) based on the charge carrier lifetime or the intrinsic carrier concentration. In contrast, photoexcitation by short laser pulses (150 ps in this work) allows direct control of the initially generated charge carrier concentration Δn . This induced carrier concentration can be calculated from the absorbed photon density per pulse and the thickness of the thin film.

The emitted photoluminescence photon flux is given for relevant conditions ($\Delta n > n_i$) by Eq. (5), which depends on k_2 , Δn and p_0 (Ref. 60),

$$Y_{\text{PL}} \approx k_2 [p_0 + \Delta n] \Delta n. \quad (5)$$

Previously, TRPL decays of lead halide perovskites were analyzed to determine the doping concentration by Staub *et al.*⁴⁵ However, the TRPL decay can be relatively complex, as it is influenced by charge carrier recombination, separation, diffusion, and extraction. To avoid modeling these processes, here, the initial TRPL amplitude rather than the decay will be analyzed using Eq. (5) for the doping concentration.

Figures 4(a) and 4(b) show the TRPL transients for a Sn-based $\text{FA}_{0.83}\text{Cs}_{0.17}\text{SnI}_3$ and for a Pb-based triple cation $\text{Cs}_{0.05}(\text{FA}_{0.83}\text{MA}_{0.17})_{0.95}\text{Pb}(\text{I}_{0.83}\text{Br}_{0.17})_3$, respectively, as the function of the injected carrier concentration.

$\text{Pb}(\text{I}_{0.83}\text{Br}_{0.17})_3$ perovskite thin films as the function of the carrier concentration, respectively. Figure 4(c) shows that, as far as pure Sn-based perovskite is concerned, the initial TRPL amplitude depends linearly on the carrier concentration, and consequently, the doping is larger than the highest induced carrier concentration of $1.4 \times 10^{16} \text{ cm}^{-3}$. Regarding the Pb-based, triple cation perovskite $\text{Cs}_{0.05}(\text{FA}_{0.83}\text{MA}_{0.17})_{0.95}\text{Pb}(\text{I}_{0.83}\text{Br}_{0.17})_3$, the initial fast decay in Fig. 4(b) becomes more pronounced with increasing intensity which means, according to the corresponding trend in Fig. 4(c), that the amplitude increases with the square of the induced carrier concentration. As a result, the doping is smaller than the smallest induced carrier concentration of $4 \times 10^{13} \text{ cm}^{-3}$. Finally, we note that the lifetime of the charges depends on their density as the recombination regime changes depending on the carrier density. This has been shown in several papers on perovskite solar cells, also in our own work, for example, in Fig. 3 of Ref. 62 (or in Refs. 60 and 65). Moreover, at the same laser fluence, the Sn-based perovskite exhibits a much faster decay than the Pb-based one, which is due to the higher doping concentration and higher defect density.

The fact that the doping density is higher in the Sn-based perovskites than in the Pb-based ones, can be also confirmed by intensity dependent PLQY measurements. As shown in supplementary material Fig. S5, we found that Q_e^{lum} plateaus indeed at low intensities below 10^{-1} suns with a doping density on the order of $2 \times 10^{14} \text{ cm}^{-3}$.

DARK CELIV

While the measurements presented above were used to estimate the doping density in neat perovskite films, in the following, we aim to quantify the doping density in device configuration. To this end, we performed CELIV measurements, which is a powerful technique that allows the user to measure doping densities as well as mobile ion densities. By using an additional pulsed laser excitation (photo-CELIV), it is also possible to assess the photogenerated carrier density.

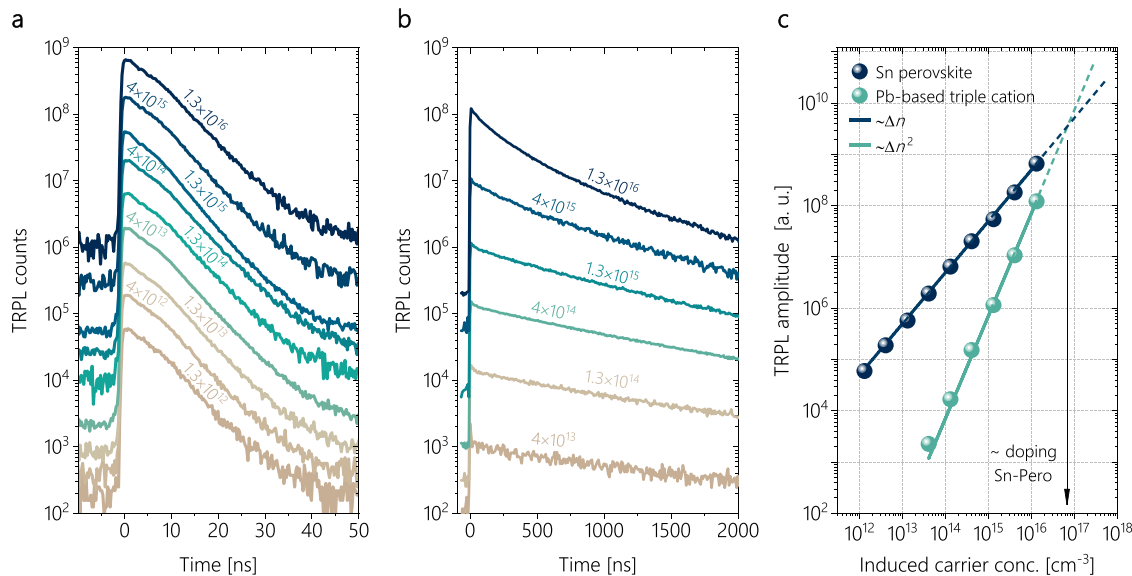


FIG. 4. (a) and (b) Injection dependent TRPL transients for a tin-based $\text{FA}_{0.83}\text{Cs}_{0.17}\text{SnI}_3$ perovskite and a lead-based triple cation perovskite $\text{Cs}_{0.05}(\text{FA}_{0.83}\text{MA}_{0.17})_{0.95}\text{Pb}(\text{I}_{0.83}\text{Br}_{0.17})_3$, respectively, as the function of the injected carrier concentration. (c) TRPL amplitude as function of injected carrier concentration corresponding to the same films as in (a) and (b).

The transient directly shows the presence of additional charges if they are present in relevant conditions with regard to the CU_{bi}/eV charge density.^{50,66,67} The latter can be controlled by adjusting the applied bias U_{max} to the metal electrodes.³⁵

In this measurement, the cell is reverse-biased by a linearly increasing voltage with amplitude U_{max} , as it is shown in Fig. 5(a). As a result of the accumulation of charges on the contacts of the solar cell, a displacement current density j_0 builds up in the RC circuit, which is subsequently measured with an oscilloscope. Previous experiments^{50,68,69} have shown that electronic charges are extracted from the device on microsecond timescales. Therefore, any doping-induced charges that are present in the active layer should be extracted at the same timescales. Their presence will be visible only if the doping-induced charge density is higher than the CU_{max}/eV (or CU_{bi}/eV if $CU_{max} = CU_{bi}$). If this is the case, a “bump” will appear on top of the CU_{max} charge, as depicted in Fig. 5(a). The integrated area under this bump corresponds to the total doping-induced charge.

As it is shown in Fig. 5(b), none of the displayed dark-CELIV transients show the bump on the microsecond timescales. Therefore, the free carriers that might be present in the active layer are not enough to make an appearance above the CU_{max} charge. However, as t_{pulse} increases, because the voltage is ramped more slowly, a rise beyond the CU_{max} charge is observed on the millisecond to second timescales. This effect is shown in the Fig. 5(c) for the range of studied compositions (the raw transients are provided in the [supplementary material](#) Fig. S9). Such a current increase at longer timescales has previously been linked to the presence of mobile ions,^{30,33,70–72} which have a much lower mobility than electronic charges. Therefore, performing CELIV measurements at longer timescales allows us to estimate the density and diffusion constant of the effective ionic concentration, as previously shown by Thiesbrummel *et al.* for PbSn perovskite systems.⁵⁰

To further prove that the CELIV technique is able to estimate doping densities in relation to CU_{max}/eV , we used photo-CELIV.⁵⁰ In this experiment, a laser pulse is used to generate free charges in the

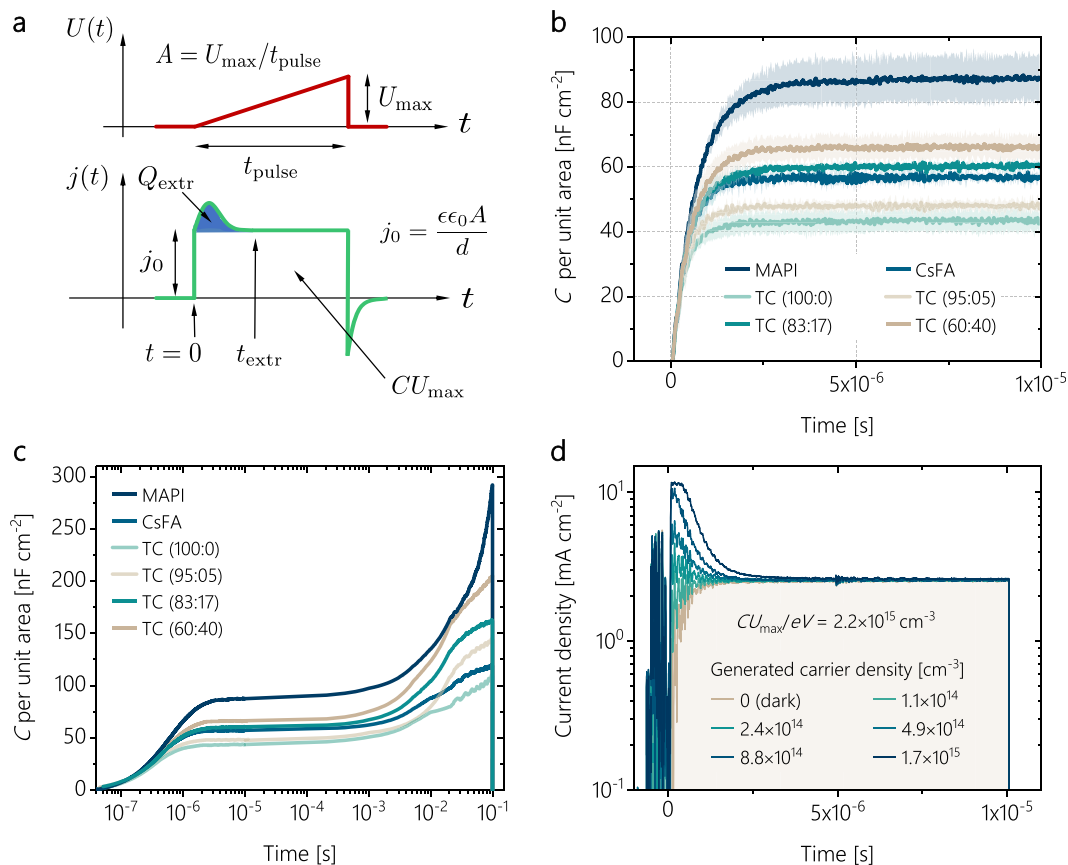


FIG. 5. (a) Schematics of the CELIV technique. The CELIV voltage ramp is applied during a time $t = t_{pulse}$ while the measured current is recorded with an oscilloscope. In the case, a free electronic charge concentration larger than CU_{bi}/eV is present, a bump on top of the CU_{max} charge can be observed during the initial phase of the extraction. The integrated area of such a bump corresponds to the total extracted charge of free electronic carriers. (b) Dark-CELIV transients for the different investigated perovskite compositions on the microsecond timescale. (c) Complete dark-CELIV transients extending to longer timescales, showing the presence of mobile ions in the range of milliseconds. (d) Photo-CELIV transients for a $Cs_{0.05}(FA_{0.83}MA_{0.17})_{0.95}Pb(I_{0.83}Br_{0.17})_3$ triple cation perovskite showing the photogenerated charge after the laser pulse excitation. The shaded area represents the CU_{max} charge, which, divided by the elementary charge e , and the cell volume V , amounts to $CU_{max}/eV = 2.2 \times 10^{15}\ cm^{-3}$. The plot mainly demonstrates that if a large enough concentration of electronic charges were present, they would show up as a bump on top of the CU_{max} charge. In this sense, the bump is always seen under illumination, whereas it would appear in the dark only if doping-induced charges are present.

device. The laser pulse is timed such that it excites these charges right when the voltage ramp starts. Using different laser fluences, a range of known free carrier concentrations can be excited in the bulk of the material. This allows us to prove that if there were enough charges in the active layer, we would in fact measure them. Hence the fact that we did not see a bump in the dark means that there are not enough charges. The result can be seen in Fig. 5(d) for different light intensities (expressed as total induced carrier density). The data displayed here was measured on a triple cation perovskite cell $\text{Cs}_{0.05}(\text{FA}_{0.83}\text{MA}_{0.17})_{0.95}\text{Pb}(\text{I}_{0.83}\text{Br}_{0.17})_3$. The transients demonstrate that when the photo-generated charge carrier density is below 10^{14} cm^{-3} , it cannot be detected. In other words, a photo-generated free charge carrier density below 10^{14} cm^{-3} is buried under the CU_{max} charge. As long as the free-charge-carrier density is high enough to be detected, the bump would always appear under illumination and it would appear in the dark only if doping-induced charges are present.

Finally, Fig. 5(d) also shows that although the doping density in equilibrium is significantly below the required threshold (CU_{bi}/eV) to influence the device performance, the mobile ion density is comparable or exceeds the CU_{bi}/eV charge density. Therefore, even though perovskites cannot be considered to have a performance-relevant doping density, mobile ions are present in concentrations large enough to form field-free regions and junctions in the devices under steady-state conditions, thereby impacting the device performance.

CONCLUSIONS

Through an extensive experimental investigation, composed of different optical and electrical experimental techniques, we collected evidence to address the controversial question of whether perovskite thin films behave like doped semiconductors. By introducing the concept of the electrode charge, we derived a critical threshold at which doping matters, which is supported by drift-diffusion simulations. For a broad range of perovskite compositions, Hall effect measurements, carried out using an AC field and lock-in detection, showed that the density of doping induced charge is between $5 \times 10^{11} - 3 \times 10^{13} \text{ cm}^{-3}$. For MAPi, this is in good agreement with earlier observations ($1.9 \times 10^{12} \text{ cm}^{-3}$) using Hall effect measurements. The electrical conductivity of the studied compositions was measured in three different ways, namely, with two-contacts, four-contacts, and with the transfer length method. The carrier mobility was calculated from the carrier density determined by the Hall effect and the four-contact conductivity. The values are between 0.5 and $2 \text{ cm}^2 \text{ V}^{-1} \text{ s}^{-1}$, which are in good agreement with those values found in the literature for similar perovskite systems. We then measured the intensity-dependent PLQY ($Q_{\text{e}}^{\text{lum}}$) and TRPL amplitudes. By these two methods, upper limits for the doping induced charge density of $2 \times 10^{12} \text{ cm}^{-3}$ and of $4 \times 10^{13} \text{ cm}^{-3}$ were deduced for Pb-based perovskites, respectively. Consequently, these results are consistent with the carrier density determined by Hall effect. While the above-mentioned measurements were conducted on bare perovskite films, we additionally used CELIV measurements to determine the doping density in full devices. The results obtained show that the doping density is lower than the charge carrier density on the electrodes CU_{max}/eV in the CELIV experiment, which amounts to $2.2 \times 10^{15} \text{ cm}^{-3}$. This also highlights that from electrical measurements, it is difficult to detect doping concentrations below the CU_{bi}/eV charge density and it is important to note that the same limitation applies to the detection of charged defects.

The consistency of these measurements allows us to conclude that the doping density is negligible for the device performance for most Pb-based perovskites. Nonetheless, for halide perovskites incorporating other metals such as Sn, which are known to easily oxidize and self-dope, doping is more likely to impact device performance. Considering that for a *pn*-junction to be formed within the active layer, the minimum doping density is approximately 10^{16} cm^{-3} , we are able to conclude that the doping densities of typically used Pb-based halide perovskites investigated in this work are not high enough to influence the internal band bending in contrast to mobile ions.

SUPPLEMENTARY MATERIAL

See the [supplementary material](#) for the fabrication methods of films and devices, the description of each one of the setups and measurements, and the [supplementary material](#) figures and tables cited in the manuscript. It also includes two notes about the Hall effect and its relation to ions as well as about the working principle of the transfer-length method.

ACKNOWLEDGMENTS

We acknowledge funding from the Deutsche Forschungsgemeinschaft (DFG, German Research Foundation) within the SPP 2196 (Nos. SURPRISE 423749265 and HIPSTER 424709669). We further acknowledge financial support by the Federal Ministry for Economic Affairs and Energy within the framework of the 7th Energy Research Programme (P3T-HOPE, 03EE1017C) and HyPerCells (a joint graduate school of the Potsdam University and the Helmholtz-Zentrum Berlin für Materialien und Energie). J.T. thanks the Rank Prize fund for financial support. M.S. further acknowledges the Heisenberg program from the Deutsche Forschungsgemeinschaft (DFG, German Research Foundation) for funding, Project No. 498155101. F.L. acknowledges financial support from the Alexander von Humboldt Foundation via the Feodor Lynen program. A.M. acknowledges financial support from the German Science Foundation (DFG) in the framework of the priority program SPP 2196. A.M. gratefully acknowledges Danny Kojda and Klaus Habicht for their assistance.

AUTHOR DECLARATIONS

Conflict of Interest

The authors have no conflicts to disclose.

DATA AVAILABILITY

The data that support the findings of this study are available from the corresponding author upon reasonable request.

REFERENCES

- ¹C. R. Abernathy, S. J. Pearton, R. Caruso, F. Ren, and J. Kovalchik, "Ultrahigh doping of GaAs by carbon during metalorganic molecular beam epitaxy," *Appl. Phys. Lett.* **55**, 1750–1752 (1989).
- ²H. J. Queisser and E. E. Haller, "Defects in semiconductors: Some fatal, some vital," *Science* **281**, 945–950 (1998).
- ³R. A. Street, "Doping and the Fermi energy in amorphous silicon," *Phys. Rev.* **49**, 1187–1190 (1982).
- ⁴C. K. Chiang *et al.*, "Electrical conductivity in doped polyacetylene," *Phys. Rev. Lett.* **39**, 1098–1101 (1977).
- ⁵I. E. Jacobs and A. J. Moulé, "Controlling molecular doping in organic semiconductors," *Adv. Mater.* **29**, 1703063 (2017).

- ⁶P. Pingel, R. Schwarzl, and D. Neher, "Effect of molecular p-doping on hole density and mobility in poly(3-hexylthiophene)," *Appl. Phys. Lett.* **100**, 143303 (2012).
- ⁷P. Pingel and D. Neher, "Comprehensive picture of p-type doping of P3HT with the molecular acceptor F4TCNQ," *Phys. Rev. B* **87**, 115209 (2013).
- ⁸I. E. Jacobs *et al.*, "Comparison of solution-mixed and sequentially processed P3HT:F4TCNQ films: Effect of doping-induced aggregation on film morphology," *J. Mater. Chem. C* **4**, 3454–3466 (2016).
- ⁹A. Musienko *et al.*, "Photo-Hall-effect spectroscopy with enhanced illumination in p -Cd_{1-x}Mn_xTe showing negative differential photoconductivity," *Phys. Rev. Appl.* **10**, 014019 (2018).
- ¹⁰R. Sandheep, U. Thomas, and K. Thomas, "Comment on 'Resolving spatial energetic distributions trap states metal halide perovskite solar cells,'" *Science* **371**, eabd8014 (2021).
- ¹¹J. Siekmann, S. Ravishankar, and T. Kirchartz, "Apparent defect densities in halide perovskite thin films and single crystals," *ACS Energy Lett.* **6**, 3244–3251 (2021).
- ¹²J. Euvrard, Y. Yan, and D. B. Mitzi, "Electrical doping in halide perovskites," *Nat. Rev. Mater.* **6**, 531–549 (2021).
- ¹³L. Huang *et al.*, "Schottky/p-n cascade heterojunction constructed by intentional n-type doping perovskite toward efficient electron layer-free perovskite solar cells," *Sol. RRL* **3**, 1800274 (2019).
- ¹⁴L. Huang and Y. Zhu, "p-n heterojunction perovskite solar cell with bilateral Ohmic contacts," *Appl. Phys. Lett.* **118**, 052105 (2021).
- ¹⁵W.-J. Yin, T. Shi, and Y. Yan, "Unusual defect physics in CH₃NH₃PbI₃ perovskite solar cell absorber," *Appl. Phys. Lett.* **104**, 063903 (2014).
- ¹⁶J. M. Ball and A. Petrozza, "Defects in perovskite-halides and their effects in solar cells," *Nat. Energy* **1**, 16149 (2016).
- ¹⁷Q. Wang *et al.*, "Qualifying composition dependent p and n self-doping in CH₃NH₃PbI₃," *Appl. Phys. Lett.* **105**, 163508 (2014).
- ¹⁸P. Cui *et al.*, "Planar p-n homojunction perovskite solar cells with efficiency exceeding 21.3%," *Nat. Energy* **4**, 150–159 (2019).
- ¹⁹A. Musienko *et al.*, "Defects in hybrid perovskites: The secret of efficient charge transport," *Adv. Funct. Mater.* **31**, 2104467 (2021).
- ²⁰J. Kim, S.-H. Lee, J. H. Lee, and K.-H. Hong, "The role of intrinsic defects in methylammonium lead iodide perovskite," *J. Phys. Chem. Lett.* **5**, 1312–1317 (2014).
- ²¹J. Euvrard, O. Gunawan, and D. B. Mitzi, "Impact of PbI₂ passivation and grain size engineering in CH₃NH₃PbI₃ solar absorbers as revealed by carrier-resolved photo-Hall technique," *Adv. Energy Mater.* **9**, 1902706 (2019).
- ²²A. Zohar *et al.*, "What is the mechanism of MAPbI₃ p-doping by I₂? Insights from optoelectronic properties," *ACS Energy Lett.* **2**, 2408–2414 (2017).
- ²³P. Schulz *et al.*, "Electronic level alignment in inverted organometal perovskite solar cells," *Adv. Mater. Interfaces* **2**, 1400532 (2015).
- ²⁴D. Shin *et al.*, "Mechanism and timescales of reversible p-doping of methylammonium lead triiodide by oxygen," *Adv. Mater.* **33**, 2100211 (2021).
- ²⁵M. Stollerfoht *et al.*, "The impact of energy alignment and interfacial recombination on the internal and external open-circuit voltage of perovskite solar cells," *Energy Environ. Sci.* **12**, 2778–2788 (2019).
- ²⁶P. Caprioglio *et al.*, "High open circuit voltages in pin-type perovskite solar cells through strontium addition," *Sustainable Energy Fuels* **3**, 550–563 (2019).
- ²⁷F. Zu *et al.*, "Unraveling the electronic properties of lead halide perovskites with surface photovoltage in photoemission studies," *ACS Appl. Mater. Interfaces* **11**, 21578–21583 (2019).
- ²⁸T. Hellmann *et al.*, "The electronic structure of MAPI-based perovskite solar cells: Detailed band diagram determination by photoemission spectroscopy comparing classical and inverted device stacks," *Adv. Energy Mater.* **10**, 2002129 (2020).
- ²⁹A. Walsh, D. O. Scanlon, S. Chen, X. G. Gong, and S. H. Wei, "Self-regulation mechanism for charged point defects in hybrid halide perovskites," *Angew. Chem., Int. Ed.* **54**, 1791–1794 (2015).
- ³⁰S. Reichert *et al.*, "Ionic-defect distribution revealed by improved evaluation of deep-level transient spectroscopy on perovskite solar cells," *Phys. Rev. Appl.* **13**, 034018 (2020).
- ³¹Y. Cheng *et al.*, "The detrimental effect of excess mobile ions in planar CH₃NH₃PbI₃ perovskite solar cells," *J. Mater. Chem. A* **4**, 12748–12755 (2016).
- ³²L. Bertoluzzi *et al.*, "Mobile ion concentration measurement and open-access band diagram simulation platform for halide perovskite solar cells," *Joule* **4**, 109–127 (2020).
- ³³M. H. Futscher *et al.*, "Quantification of ion migration in CH₃NH₃PbI₃ perovskite solar cells by transient capacitance measurements," *Mater. Horiz.* **6**, 1497–1503 (2019).
- ³⁴T. Kirchartz *et al.*, "Sensitivity of the Mott-Schottky analysis in organic solar cells," *J. Phys. Chem. C* **116**, 7672–7680 (2012).
- ³⁵O. J. Sandberg, M. Nyman, and R. Österbacka, "Direct determination of doping concentration and built-in voltage from extraction current transients," *Org. Electron.* **15**, 3413–3420 (2014).
- ³⁶O. Almora, C. Aranda, E. Mas-Marzá, and G. Garcia-Belmonte, "On Mott-Schottky analysis interpretation of capacitance measurements in organometal perovskite solar cells," *Appl. Phys. Lett.* **109**, 173903 (2016).
- ³⁷J. Diekmann *et al.*, "Pathways toward 30% efficient single-junction perovskite solar cells and the role of mobile ions," *Sol. RRL* **5**, 2100219 (2021).
- ³⁸L. B. Valdes, "Resistivity measurements on germanium for transistors," *Proc. IRE* **42**, 420–427 (1954).
- ³⁹G. K. Reeves and H. B. Harrison, "Obtaining the specific contact resistance from transmission line model measurements," *IEEE Electron Device Lett.* **3**, 111–113 (1982).
- ⁴⁰L. J. van der Pauw, "A method of measuring specific resistivity and Hall effect of discs of arbitrary shape," *Philips Res. Rep.* **13**, 1–9 (1958).
- ⁴¹D. K. Schroder, *Semiconductor Material and Device Characterization* (John Wiley & Sons, 2006).
- ⁴²S. Ravishankar, Z. Liu, and T. Kirchartz, "Multilayer capacitances: How selective contacts affect capacitance measurements of perovskite solar cells," *arXiv:2106.05758* (2021).
- ⁴³O. Gunawan *et al.*, "Carrier-resolved photo-Hall effect," *Nature* **575**, 151–155 (2019).
- ⁴⁴S. Feldmann *et al.*, "Photodoping through local charge carrier accumulation in alloyed hybrid perovskites for highly efficient luminescence," *Nat. Photonics* **14**, 123–128 (2020).
- ⁴⁵F. Staub *et al.*, "Beyond bulk lifetimes: Insights into lead halide perovskite films from time-resolved photoluminescence," *Phys. Rev. Appl.* **6**, 044017 (2016).
- ⁴⁶T. J. Savenije, D. Guo, V. M. Caselli, and E. M. Hutter, "Quantifying charge-carrier mobilities and recombination rates in metal halide perovskites from time-resolved microwave photoconductivity measurements," *Adv. Energy Mater.* **10**, 1903788 (2020).
- ⁴⁷J. Kniepert, I. Lange, N. J. van der Kaap, L. J. A. Koster, and D. Neher, "A conclusive view on charge generation, recombination, and extraction in as-prepared and annealed P3HT:PCBM blends: Combined experimental and simulation work," *Adv. Energy Mater.* **4**, 1301401 (2014).
- ⁴⁸V. M. Le Corre *et al.*, "Revealing charge carrier mobility and defect densities in metal halide perovskites via space-charge-limited current measurements," *ACS Energy Lett.* **6**, 1087–1094 (2021).
- ⁴⁹G. Juška, K. Arlauskas, M. Viliūnas, and J. Kočka, "Extraction current transients: New method of study of charge transport in microcrystalline silicon," *Phys. Rev. Lett.* **84**, 4946–4949 (2000).
- ⁵⁰J. Thiesbrummel *et al.*, "Universal current losses in perovskite solar cells due to mobile ions," *Adv. Energy Mater.* **11**, 2101447 (2021).
- ⁵¹T. Kirchartz and D. Cahen, "Minimum doping densities for p-n junctions," *Nat. Energy* **5**, 973–975 (2020).
- ⁵²J. Hüpkes, U. Rau, and T. Kirchartz, "Dielectric junction: Electrostatic design for charge carrier collection in solar cells," *Sol. RRL* **6**, 2100720 (2021).
- ⁵³B. Das, I. Aguilera, U. Rau, and T. Kirchartz, "Effect of doping, photodoping and bandgap variation on the performance of perovskite solar cells," *arXiv:2112.03445* (2021).
- ⁵⁴M. Burgelman, J. Verschraegen, S. Degraeve, and P. Nollet, "Modeling thin-film PV devices," *Prog. Photovoltaics* **12**, 143–153 (2004).
- ⁵⁵M. Burgelman, P. Nollet, and S. Degraeve, "Modelling polycrystalline semiconductor solar cells," *Thin Solid Films* **361–362**, 527–532 (2000).
- ⁵⁶A. Musienko *et al.*, "Deep levels, charge transport and mixed conductivity in organometallic halide perovskites," *Energy Environ. Sci.* **12**, 1413–1425 (2019).
- ⁵⁷E. A. Duijnste *et al.*, "Toward understanding space-charge limited current measurements on metal halide perovskites," *ACS Energy Lett.* **5**, 376–384 (2020).

- ⁵⁸W. Peng *et al.*, “Quantification of ionic diffusion in lead halide perovskite single crystals,” *ACS Energy Lett.* **3**, 1477–1481 (2018).
- ⁵⁹J. W. Orton and M. J. Powell, “The Hall effect in polycrystalline and powdered semiconductors,” *Rep. Prog. Phys.* **43**, 1263–1307 (1980).
- ⁶⁰T. Kirchartz, J. A. Márquez, M. Stolterfoht, and T. Unold, “Photoluminescence-based characterization of halide perovskites for photovoltaics,” *Adv. Energy Mater.* **10**, 1904134 (2020).
- ⁶¹S. Feldmann *et al.*, “Tailored local bandgap modulation as a strategy to maximize luminescence yields in mixed-halide perovskites,” *Adv. Opt. Mater.* **9**, 2100635 (2021).
- ⁶²C. M. Wolff *et al.*, “Orders of recombination in complete perovskite solar cells: Linking time-resolved and steady-state measurements,” *Adv. Energy Mater.* **11**, 2101823 (2021).
- ⁶³T. Kirchartz, L. Krückemeier, and E. L. Unger, “Research update: Recombination and open-circuit voltage in lead-halide perovskites,” *APL Mater.* **6**, 100702 (2018).
- ⁶⁴J. M. Richter *et al.*, “Enhancing photoluminescence yields in lead halide perovskites by photon recycling and light out-coupling,” *Nat. Commun.* **7**, 13941 (2016).
- ⁶⁵E. Gutierrez-Partida *et al.*, “Large-grain double cation perovskites with 18 μ s lifetime and high luminescence yield for efficient inverted perovskite solar cells,” *ACS Energy Lett.* **6**, 1045–1054 (2021).
- ⁶⁶G. Juška, N. Nekrašas, V. Valentinavičius, P. Meredith, and A. Pivrikas, “Extraction of photogenerated charge carriers by linearly increasing voltage in the case of Langevin recombination,” *Phys. Rev. B* **84**, 155202 (2011).
- ⁶⁷G. Juška *et al.*, “Charge transport in pi-conjugated polymers from extraction current transients,” *Phys. Rev. B* **62**, R16235–R16238 (2000).
- ⁶⁸M. Stolterfoht *et al.*, “Approaching the fill factor Shockley–Queisser limit in stable, dopant-free triple cation perovskite solar cells,” *Energy Environ. Sci.* **10**, 1530–1539 (2017).
- ⁶⁹D. Kiermasch *et al.*, “Unravelling steady-state bulk recombination dynamics in thick efficient vacuum-deposited perovskite solar cells by transient methods,” *J. Mater. Chem. A* **7**, 14712–14722 (2019).
- ⁷⁰M. Fischer, K. Tvingstedt, A. Baumann, and V. Dyakonov, “Doping profile in planar hybrid perovskite solar cells identifying mobile ions,” *ACS Appl. Energy Mater.* **1**, 5129–5134 (2018).
- ⁷¹N. Wu, D. Walter, A. Fell, Y. Wu, and K. Weber, “The impact of mobile ions on the steady-state performance of perovskite solar cells,” *J. Phys. Chem. C* **124**, 219–229 (2020).
- ⁷²O. Almora *et al.*, “Capacitive dark currents, hysteresis, and electrode polarization in lead halide perovskite solar cells,” *J. Phys. Chem. Lett.* **6**, 1645–1652 (2015).